Impact of reversible proton insertion on the electrochemistry of electrode materials operating in mild aqueous electrolytes: a case study with TiO₂

Nikolina Makivić, Kenneth D. Harris, Jean-Marie Tarascon, Benoît Limoges* and Véronique Balland*

N. Makivić, B. Limoges, V. Balland

Université Paris Cité, CNRS, Laboratoire d'Electrochimie Moléculaire, F-75013 Paris, France
E-mail: limoges@u-paris.fr ; veronique.balland@u-paris.fr

K. D. Harris

National Research Council of Canada, Nanotechnology Research Centre, 11421
Saskatchewan Drive, Edmonton, Alberta T6G 2M9, Canada

Department of Mechanical Engineering, University of Alberta, Edmonton, Alberta T6G 2V4, Canada

J-M. Tarascon

Chimie du Solide et de l'Energie, UMR 8260, Collège de France, 11 Place Marcelin
Berthelot, 75231 Paris Cedex 05, France

Abstract

Near-neutral aqueous electrolytes are to be preferred for the development of sustainable electrochemical energy conversion and storage devices. Protons are inherent to these electrolytes and their reactivity towards the electrode material extends beyond their own reduction, especially when reversible proton insertion takes place in the bulk electrode material from acidic or buffered electrolytes. However, a still burning question regards whether reversible proton insertion persists when working in unbuffered mild aqueous electrolytes, and if so, with which consequences on the functioning of the electrode material. Here, we address this issue by examining TiO_2 as a model insertion electrode in a range of mild aqueous electrolytes. Through a combination of experiments, modelling and multiphysics simulations, we demonstrate that, in a KCl-based electrolyte, water acts as proton donor to support reversible insertion of protons in TiO_2, while in a NH_4Cl-based aqueous electrolyte, the proton donor is NH_4^+. Moreover, we establish that strong pH gradients develop at the electrode interface during proton insertion/disinsertion, highlighting their dependence on the proton donor/acceptor and rationalizing their impact on the electrode voltage. Overall, this work provides a comprehensive framework of proton-insertion coupled electron transfer (PICET) that can be easily generalised to other electrode materials.

1. Introduction

Aqueous electrolytes are at the base of a myriad of technological applications in energy conversion and storage. Compared to non-aqueous electrolytes, aqueous electrolytes often allow large-scale, low-cost technological developments with reduced environmental impact and improved safety.[1,2] Another essential attribute is that proton-coupled electron transfer (PCET) reactions are inherent to these media, defining both the electrochemical stability domain of the electrolyte and also the reactions of interest, *e.g.*, the production of dihydrogen in photoelectrochemical cells *via* photo- and/or electrochemical water splitting, or the production of electricity in fuel cells *via* electrochemical transformation of H_2 and O_2 into water.[3],[4] This is also true with electrochemical energy storage devices, notably aqueous batteries relying on PCET processes such as the reversible proton-coupled electrodissolution reaction at the PbO_2 cathode in lead-acid batteries[5] or the reversible proton insertion-coupled electron transfer (PICET) reaction at the NiOOH cathode of alkaline NiCd or NiMH batteries.[6] Such reversible proton insertions in bulk electrode materials are even more widespread than initially thought. Indeed, their occurrence has now been demonstrated for materials ranging from metal oxides, polyanionic frameworks, hexacyanoferrates, and organic entities.[7] In most cases, fast charge/discharge rate capabilities were reported and attributed to the unique properties of protons as charge carriers, which on account of their small size and high reactivity can lead to rapid insertion/disinsertion kinetics as well as fast solid-state diffusion/migration across the active electrode material, driving thus the renaissance of the so-called proton batteries.[8]

Overall, the majority of aqueous-based energy storage and conversion technologies operate under harsh acidic or basic conditions, which can lead to corrosion issues that limit long-term stability. A straightforward strategy to overcome this concern is developing technologies capable of operation in neutral or weakly acidic/basic electrolytes. However, to move in this direction it is essential to carefully reassess the nature of proton donors/acceptors involved in the PCET/PICET reactions, and also to properly gauge their influence over thermodynamics and kinetics. Additionally, because of the low concentrations of either hydronium or hydroxide ions in the preferred pH-range from 4 to 10, PCET/PICET reactions in unbuffered aqueous electrolytes are expected to lead to pH gradients at electrode interfaces. These different aspects were well-identified in energy-conversion systems involving irreversible PCETs, especially in electrochemical cells used for water electrolysis or photoelectrochemical water splitting.[9–17] However, it has never been clearly established in PICET-based energy storage systems. Indeed, the question of the source of protons in batteries operating in mild unbuffered aqueous electrolytes has been largely overlooked, often with the assumption that water plays the role of

an inexhaustible source of protons, which has never been unambiguously demonstrated and also is not necessarily true.

In our previous work on proton insertion in amorphous TiO_2, we revealed the strong dependence of charge storage on the chemical composition of the aqueous electrolyte.[18] We also showed that while the reversible insertion of protons in TiO_2 is massive in a pH 7 buffered aqueous electrolyte, it turns out to be negligible (over the same potential window) when cycled in a neutral electrolyte made only of water and an inert salt.[18] We ascribed this to the inability of water to deliver protons to compensate the negative charges injected in TiO_2, a behaviour which can be explained by the very weak Brønsted acidity of water ($pK_a = 14$). Since then, we evidenced proton insertion in TiO_2 from unbuffered aqueous electrolytes containing a multivalent metal cation like Al^{3+} or Zn^{2+},[19] and we demonstrated that protons are delivered by the solvated hexaaquo metal cation complexes (*i.e.*, $[M(H_2O)_6]^{n+}$, where M is a multivalent metal cation) presenting a weak Brønsted acidity.[20] We thereby refuted the previously reported assumption that Al^{3+} or Zn^{2+} cations can reversibly insert in TiO_2.[19] It is thus clear that regardless of the importance in identifying the true charge carriers in electrode materials when operating in unbuffered aqueous electrolytes,[21] the origin of protons involved in the increasingly reported PICET reactions remains to be clarified. Among the key questions to address is whether the reversible insertion of protons is achievable when water is the only proton source, and if so, what consequences does this have on the thermodynamics and kinetics of the electrochemical process.

To answer these seminal questions, we herein embark in a survey exploration of reversible H^+ insertion into TiO_2 in a variety of mild aqueous electrolytes differing in chemical composition and pH. We selected nanostructured amorphous TiO_2 as it allows for efficient reversible bulk proton insertion according to the following general PICET reaction:[18,19,22]

$$TiO_2 + x\,e^- + x\,H^+ \rightleftarrows TiO_2H_x \qquad (x \text{ up to } 0.45) \qquad (1)$$
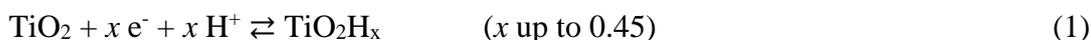
Furthermore, on the basis of an early study establishing the Pourbaix diagram of TiO_2,[23] this PICET reaction is expected to remain valid over the entire accessible pH range in water. Consequently, it is anticipated that reduced TiO_2 is able to extract protons from electrolytes containing Brønsted acids of very different strengths, and this extraction should occur without significant loss of capacity during cycling due to the intrinsic chemical stability and corrosion resistance of TiO_2 over a wide pH range. An additional interest in TiO_2 is its widespread use in energy conversion systems operating in aqueous electrolytes (the photo-(electro)chemical cells used for water or CO_2 splitting are good examples[24]). In such devices, we anticipate that the insertion of protons may interfere in the PCET reactions associated with energy conversion,

4

which has only been rarely considered. We can cite the work of Meyer's group who have shown the importance of PICET processes in photoreduced TiO_2 nanoparticles,[25] or the work of Mallouk and coll. who reported a decrease of the water-splitting efficiency at dye-sensitized TiO_2 solar cells due to proton intercalation.[26] In our group, we also revealed the faradaic interplay between the reversible insertion of protons in TiO_2 and the catalytic reduction of O_2 *via* an iron porphyrin immobilized within the mesoporous structure of a TiO_2 electrode.[27] More recently, the Augustyn and Mpourmpakis/McKone groups have both suggested that protons inserted into WO_3 govern the reactivity towards the hydrogen evolution reaction.[28,29] All these elements reinforce the idea that there is a crucial need to elucidate the key factors governing PICET reactions, and more specifically in aqueous unbuffered media. This is of prime interest for the development/optimization of not only water-based electrochemical charge storage devices, but also of many water-based energy conversion systems.

2. Results and discussion

2.1. GLAD-TiO$_2$ electrodes

In the present work, we have chosen to reinvestigate the mesoporous amorphous TiO_2 thin film (1-μm thick) model electrodes we previously used.[18,19,22] These electrodes were fabricated by glancing angle deposition (GLAD) over either a flat conductive Ti-coated or transparent FTO-coated glass substrate (as will be shown, the latter are useful for spectroelectrochemical experiments - see Experimental Section). This physical vapour deposition method allows for the preparation of highly reproducible 3D nanostructured metal oxide films, whose morphology and thickness can be well-controlled. The as-prepared 1-μm-thick GLAD-TiO_2 film consists of an array of nanocolumns extending perpendicularly from the conductive substrate (Figure S1), a morphology allowing for an easy access of the electrolyte to the interior surface of TiO_2. Furthermore, the electrode's nanosized constitutive particles (~4 nm-average diameter) allows for a particularly fast and reversible bulk proton insertion.[22] The GLAD-TiO_2 electrodes were systematically covered by a Nafion film coating in order to reduce the HER and improve the electrode cyclability, without affecting the accessibility of the electrolyte to the active material.[[22]]

2.2. Buffered aqueous electrolytes

The amorphous GLAD-TiO_2 electrodes were first characterized in aqueous buffers of different composition and pH. In **Figure 1A**, the galvanostatic charge/discharge cycles recorded in a 1 M

acetate buffer of pH 5 confirmed that the charge storage mechanism at the TiO_2 electrode occurs through the following reversible interfacial PICET reaction:[18,22]

$$TiO_2 + x\, e^- + x\, AH \leftrightarrows TiO_2H_x + x\, A^- \tag{2}$$

where AH and A^- are the weak Brønsted acid and conjugate base of the buffer, respectively (it should be noted here that the AH/A^- is in a generic notation and therefore does not necessarily reflect the chemical nature of the buffer couple and, notably, its charge).

Given the slow rate employed here (*i.e.*, 0.36 mA/cm^2, which is equivalent to 1.4 A/g or 9.5 C), the faradaic charging/discharging process is almost exclusively governed by thermodynamics,[22] which means that the potentiometric charge/discharge curves can be described by the following Nernst equilibrium potential:

$$E_{eq} = E^0_{TiO_2/TiOOH} - 2.302\frac{RT}{F}pH + \frac{RT}{F}\ln\frac{1-\theta}{\theta} + \frac{RT}{F}g(1-\theta) \tag{3}$$

or alternatively by:

$$E_{eq} = E^0_{TiO_2/TiOOH} - 2.302\frac{RT}{F}\left(pK_a - \log\frac{a_{A^-}}{a_{AH}}\right) + \frac{RT}{F}\ln\frac{1-\theta}{\theta} + \frac{RT}{F}g(1-\theta) \tag{4}$$

where $E^0_{TiO_2/TiOOH}$ is the standard potential of the $Ti^{IV}O_2/Ti^{III}OOH$ redox couple at pH = 0 (*i.e.*, $E^0_{TiO_2/TiOOH}$ = -0.94 V *vs.* SCE[22]), a_{A^-} and a_{AH} are the base and acid activities, θ is the state of protonation assuming that a value of 1 corresponds to the maximal charge (*i.e.*, $x \sim$ 0.5 in **equation 2**),[22] g is the Frumkin parameter reflecting the mean interaction energy between the insertion sites[30] (*i.e.*, positive for repulsion and negative for attraction – a g value of +16 was previously estimated by us for amorphous TiO_2[22]), F *is* the Faraday constant (96 485 C/mol), T is the temperature in K, and R is the universal gas constant (8.314 J·mol/K). The theoretical galvanostatic curve drawn from **equation 3** using $g = 16$ and pH = 5 is overlaid in Figure 1 (dashed line). Although only valid for ideal behaviour (free of voltage hysteresis and entirely governed by thermodynamics), it compares well with the experimental charge/discharge curves (especially in terms of slope and potential position). The main difference is the voltage hysteresis observed in the experimental cycles, which likely results from the Ohmic drop brought on by the Nafion coating (*vide infra*). Another divergence between the experimental and theoretical curves is observed when the discharge potential reaches a sufficiently negative value so that the hydrogen evolution reaction (HER) begins to interfere. HER interference was experimentally verified by the poor Coulombic efficiency (*CE* = 87%) and also by the formation of small bubbles at the electrode. However, the HER can be largely avoided by limiting the charge to half its maximal value, *i.e.* Q_c = 80 mA·h·g^{-1} (and $x =$

6

0.25 in equation 2). Under these moderate accumulation conditions (blue curve in Figure 1A), a much better *CE* of 97% was achieved. These experimental conditions were thus selected for further studies in the different buffered aqueous electrolytes with pHs ranging from 5 to 12.2 (see Experimental Section for details).
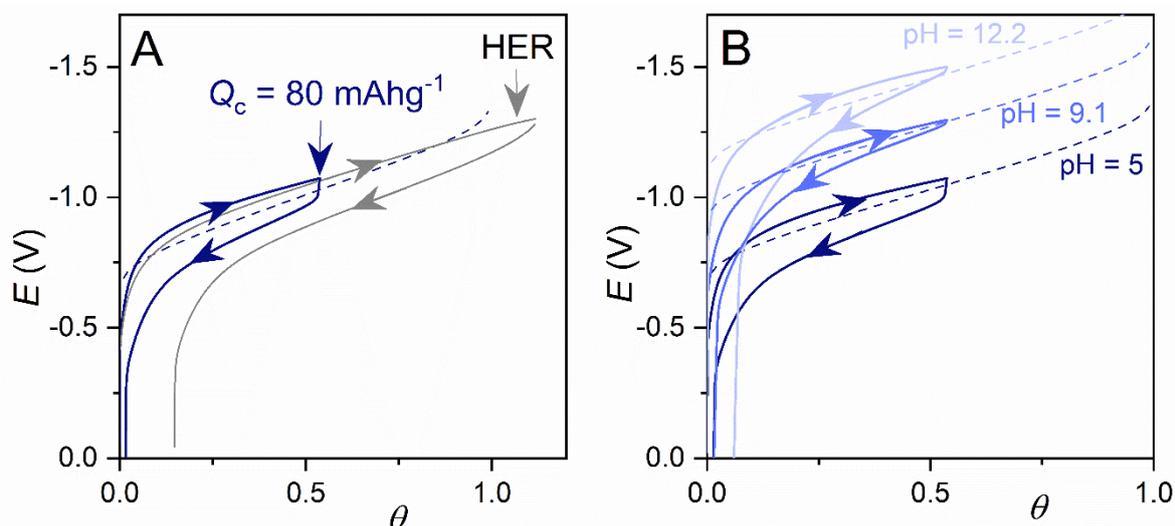

Figure 1. Comparison of (solid lines) experimental and (dashed lines) theoretical galvanostatic charge/discharge cycles recorded at a Nafion-coated GLAD-TiO$_2$/Ti electrode in buffered electrolytes (rate: 0.36 mA/cm^2). (A) Data recorded in a 1 M acetate buffer at pH 5 with a maximum charge fixed at (blue) 80 or (grey) 165 mA·h/g. (B) Data recorded in buffered electrolytes of (dark blue) pH 5, (blue) pH 9.1 and (light blue) pH 12.2. The theoretical dashed curves were obtained from equation 3 using the following parameters: $E^0_{\text{TiO}_2/\text{TiOOH}}$ = -0.94 V (*vs.* SCE) and g = +16. Potentials are *vs.* SCE.

Regardless of the buffered electrolyte, the galvanostatic cycles recorded at different pHs (Figure 1B and **Figure 2**) exhibit nearly identical apparent monophasic behaviour during charge and discharge, differing only by a homothetic shift of the potential to increasingly negative values as the pH increases. The *CE*s > 95 % confirm the reversibility of charge storage (with minor HER contribution) in all buffers. The potentials recorded at the end of the charge process (*i.e.*, at θ = 0.5) or at half-discharge (*i.e.*, at $\theta \sim 0.25$) depend linearly on pH (Figure 2C), with slopes of -60 mV *per* pH unit, which is close to the theoretical value predicted by the Nernst equation 3 (*i.e.*, -58 mV *per* pH unit at 20°C – see also Figure 1B). Overall, these results agree with the one-electron one-proton transfer concept in equation 2, and attest to its validity over the entire pH range explored, regardless of the chemical nature and composition of the buffer.
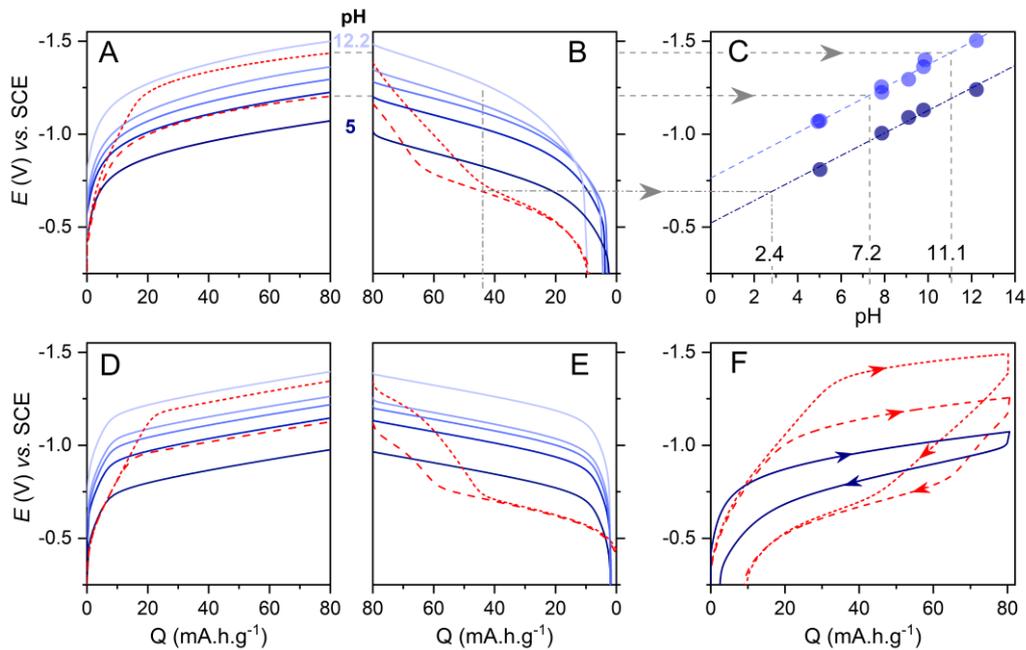
Figure 2. Galvanostatic (A) charge and (B) discharge curves (rate: 1.4 A/g) recorded at a Nafion-coated GLAD-TiO$_2$/Ti electrode in different aqueous electrolytes: (solid lines from dark to light blue) buffered electrolytes with pHs of 5.0, 7.9, 9.1, 9.8, and 12.2 (see Experimental Section for compositions), and (dashed/short-dashed red lines) unbuffered electrolytes containing either (dashed red lines) 0.4 M NH$_4$Cl or (short-dashed red lines) 0.5 M KCl (both adjusted to pH 5.0). (C) pH-dependence of the potential measured (blue dots) at the end of the charging processor (navy dots) at half-discharge. The dashed navy and blue lines are the linear regression fits, leading to slopes of -60 mV/pH unit. Theoretical galvanostatic (D) charge and (E) discharge curves (see SI and text for details) obtained from numerical simulations of the different buffered and unbuffered conditions used in panels A and B (same color code). (F) Alternative representations of the experimental galvanostatic charge/discharge cycles obtained in (solid navy line) 1 M acetate buffer (pH 5.0), (dashed red line) 0.4 M NH$_4$Cl, and (short-dashed red line) 0.5 M KCl. This representation better highlights the voltage hysteresis.

2.3. Unbuffered aqueous electrolyte containing NH$_4^+$ as weak Brønsted acid

The GLAD-TiO$_2$ electrodes were next investigated in a 0.4 M NH$_4$Cl aqueous electrolyte (adjusted to pH 5.0) supplemented with 0.5 M KCl (to maintain an ionic strength similar to that of the buffered electrolytes). This unbuffered electrolyte thus contains a large excess of the weak Brønsted acid NH$_4^+$ (pK_a = 9.25 at 25°C)[31] and negligible amounts of free protons (*i.e.*, H$_3$O$^+$) and conjugate base NH$_3$ (see the theoretical speciation diagram reported in Figure S2). Consequently, the PICET charge storage mechanism in this electrolyte should *a priori* adhere to the following electrochemical process:

$$TiO_2 + x\,e^- + x\,NH_4^+ \leftrightharpoons TiO_2H_x + x\,NH_3 \tag{5}$$

8

The shapes of the corresponding charge/discharge curves (Figure 2, dashed red lines) as well as the potential hysteresis (Figure 2F) drastically differ from those previously recorded in buffered electrolytes. Indeed, both charge and discharge curves present a distinct biphasic behaviour. Initially, the charging curves show a rapid rise in potential toward negative values (up to $Q_c \sim 10$ mA·h/g), until they curves begin to flatten and converge with the charging curves previously recorded in buffered electrolytes (almost overlapping with the discharge curve recorded in the buffer of pH 7.9). The subsequent discharge presents an almost mirror-image, leading to a large voltage hysteresis. As will be demonstrated below, this large hysteresis is the consequence of a significant pH change near the electrode/electrolyte interface. Indeed, according to equation 2, the reversible proton insertion/disinsertion at the TiO$_2$/electrolyte interface is coupled to the local consumption/production of AH/A$^-$ (here NH$_4^+$/NH$_3$), thus producing concentration gradients of these species which extend into the diffusion-convection layer normal to the electrode/electrolyte interface (see **Scheme 1**). At the metal oxide electrode surface (*i.e.*, at $z = 0$), the pH value thus relies on the relative local activities of AH (*i.e.*, NH$_4^+$) and A$^-$ (*i.e.*, NH$_3$) as follows (see SI for details):

$$\text{pH}_{z=0} = \text{p}K_a + \log\left(\frac{a_{\text{A}^-}}{a_{\text{AH}}}\right)_{z=0} \approx \text{p}K_a + \log\left(\frac{\left[\text{A}^-\right]_{z=0}}{\left[\text{AH}\right]_{z=0}}\right) \tag{6}$$

where $\left[\text{A}^-\right]_{z=0}$ and $\left[\text{AH}\right]_{z=0}$ are the concentrations of the weak base and weak acid, respectively, at $z = 0$.

Considering the time scale of the galvanostatic experiment (typically 200 s to reach the set charge of 80 mA·h/g at 0.36 mA/cm^2) and assuming a semi-infinite linear diffusion, the thickness δ of the diffusion layer is expected to extend up to ~0.1 cm normal to the electrode surface (assigning identical diffusion coefficients for NH$_4^+$ and NH$_3$ of $D = 2 \times 10^{-5}$ cm^2/s at 20°C[31] and applying $\delta = \sqrt{\pi D t}$). This distance is even overestimated compared to the thickness of the stagnant diffusion layer (δ_{max}) imposed by natural convection and from which a transition to a stationary regime is expected (with δ_{max} capped to ~ 250 µm for a species with a diffusion coefficient of 6×10^{-6} cm^2/s in an aqueous solution at 20°C).[32] Under such a stationary regime, nearly symmetric steady-state gradients of [NH$_4^+$] and [NH$_3$] develop near the electrode, leading to almost constant values of [NH$_4^+$]$_{z=0}$ and [NH$_3$]$_{z=0}$ and, consequently, to stabilization of the local pH (pH$_{z=0}$). It thus results in an equilibrium charge/discharge potential given by the following Nernst equation (for its derivation see SI and equation S21 and S22):
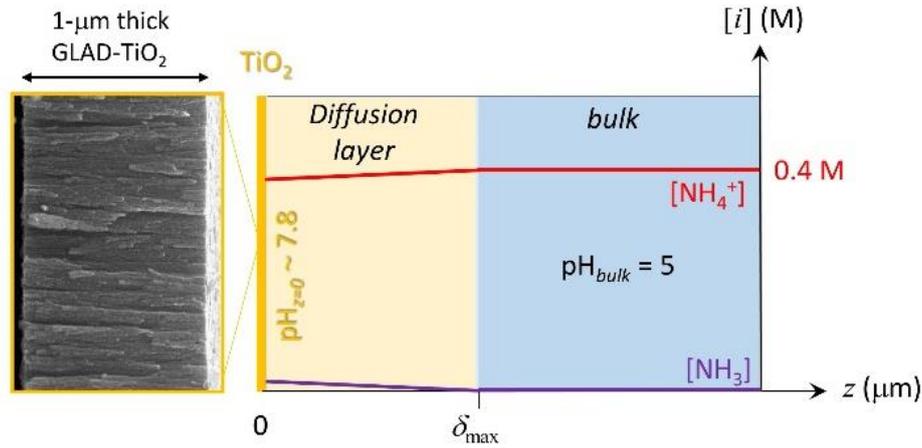
Scheme 1. Schematic representation of the steady-state concentration profiles of acid (NH_4^+) and base (NH_3) which develop at the GLAD-TiO$_2$ electrode during a galvanostatic charge (proton insertion) in the unbuffered NH$_4$Cl electrolyte. Note that because the thickness of the GLAD-TiO$_2$ film (1 µm-thick) is small relative to the thickness of the diffusion-convection layer (~200-500 µm, *vide infra*), we can depict the mesoporous electrode (of geometric area S) as a very thin film located at $z = 0$, towards which the soluble species in the electrolyte perpendicularly diffuse.

$$E_{eq} = E^0_{TiO_2/TiOOH} - 2.302\frac{RT}{F}pH_{z=0} + \frac{RT}{F}\ln\frac{1-\theta}{\theta} + \frac{RT}{F}g(1-\theta) \tag{7}$$

These simple considerations help to explain why, after a time lapse of ~ 40 s (corresponding to $Q_c \sim 14$ mA·h/g), the charge curve in the unbuffered NH$_4$Cl electrolyte finally merges with that recorded in the HEPES buffer electrolyte at pH 7.9. Considering the dependence of δ_{max} on the diffusion coefficient ($\delta_{max} \propto D^{1/4}$),[32] we used in **equation 8** (see SI for its derivation) a δ_{max} value of 340 µm for NH_4^+ (assuming a D value of 2×10^{-5} cm^2/s at 20°C) in order to estimate the local pH$_{z=0}$ under steady-state conditions.

$$pH_{z=0} = pK_a + \log\left(\frac{\frac{|i|\delta_{max}}{FSD}}{\left[NH_4^+\right]_{bulk}}\right) \tag{8}$$

Using our conditions ($pK_a = 9.25$, $[NH_4^+]_{bulk} = 0.4$ M and $i = 0.36$ mA/cm^2), a pH$_{z=0}$ of 7.4 was calculated. This value agrees with the pH of 7.2 retrieved by plotting the electrode potentials measured at the end of charge on the pH "calibration" curve in Figure 2C. It is significantly higher than that of the bulk electrolyte (pH 5.0), but remains below the pH buffer zone of the NH_4^+/NH_3 couple (ranging from pH 8.2 to 10.2 – see Figure S2) simply because the $[NH_4^+]_{z=0}/[NH_3]_{z=0}$ ratio in **equation 6**, remains below 0.1 (despite a *ca.* 3 order of magnitude increase in the local NH$_3$ concentration). Having established that the local pH increases by more

10

than two units upon proton insertion, we can conclude that the potential shift observed at the onset of charging is related to a significant local pH increase in the unbuffered electrolyte. During the subsequent discharge (dashed red line in Figure 2B), the electrode potential first increases rapidly, indicating a decrease of the local pH, and next follows a discharge curve parallel to those obtained in buffered electrolytes. The potential value reached at mid-discharge can be used to estimate the local pH by comparing to the pH "calibration" curve of Figure 2C. A value of $pH_{z=0} = 2.4$ is read, which indicates a strong local acidification of the electrolyte. At first sight, this observation may appear surprising because, if one assumes a perfectly reversible electrochemical process, one would expect to recover the initial pH at the end of the galvanostatic cycle (*i.e.*, once electrogenerated NH_3 has been fully reprotonated). However, it should be noted that our geometric cell configuration involves a large volume of electrolyte relative to the TiO_2 electrode area, so that a large fraction of NH_3 is irreversibly lost by diffusion, far into the bulk of the electrolyte (and well beyond the diffusion-convection layer). Accordingly, once the NH_3 remaining in the diffusion-convection layer is reprotonated to NH_4^+, further discharge can only proceed according to the following proton disinsertion-coupled electron transfer reaction:

$$TiO_2H_x + x\,H_2O \;\rightarrow\; TiO_2 + x\,e^- + x\,H_3O^+ \qquad\qquad (9)$$
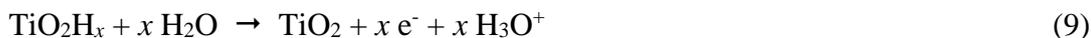
involving thus water as a proton acceptor (or Brønsted base). The consequence of this electrochemical reaction is a significant acidification of the TiO_2/electrolyte interface through local production of the strong acid H_3O^+ ($pK_a = 0$). Once a new stationary regime imposed by natural convection is established (a balance between the flux of electrogenerated H_3O^+ and H_3O^+ lost by diffusion), the local pH stabilizes.

An interesting outcome of the analysis above is confirmation that NH_4^+ enables reversible bulk proton insertion in TiO_2, which echoes our previous study on MnO_2 where we evidenced NH_4^+ driving the proton-coupled electrodissolution of solid MnO_2 to soluble Mn^{2+}.[33] From a more general perspective, these results demonstrate that aqueous NH_4^+-based electrolytes are well-suited for triggering proton insertion in metal oxides through a mechanism where the charge carrier in the electrode material (*i.e.*, H^+) differ from the charge carriers in the electrolyte (*i.e.*, NH_4^+). This is in stark contrast to a body of works concluding on the reversible insertion of NH_4^+ into various metal oxide and non-oxide electrode materials when cycled in aqueous NH_4^+-based electrolytes[34] (this has notably been reported for materials such as titanate,[35] V-based oxides,[36,37] MoO_3[38] and MnO_x[39]). The present results finally make it clear that it is essential to consider the proton-donating nature of NH_4^+ (or any other protonated amine) before

considering that this cation can be used to compensate for negative charges injected into an electrode material.

2.4. Unbuffered aqueous electrolyte containing only H$_2$O as weak Brønsted acid

A particularly simple and interesting case of unbuffered aqueous electrolyte occurs when only water and an inert supporting electrolyte (*i.e.*, 0.5 M KCl) are present. In such an electrolyte, the two reversible PICET reactions that may occur at the GLAD-TiO$_2$ electrode are:

$$TiO_2 + x\,e^- + x\,H_2O \leftrightarrows TiO_2H_x + x\,OH^- \tag{10}$$

$$TiO_2 + x\,e^- + x\,H_3O^+ \leftrightarrows TiO_2H_x + x\,H_2O \tag{11}$$

For the first reaction (**equation 10**), the weak proton donor is the solvent water (characterized by an activity equal to 1 and a pK_a of 14), which generates the strong hydroxide base, while, for the second reaction (**equation 11**), the proton source is H$_3$O$^+$ arising from the self-ionization of water. This second reaction, however, cannot take place during TiO$_2$ charging in electrolytes at near-neutral pH because of the too low concentration of H$_3$O$^+$ (~10^{-5} M of H$_3$O$^+$ in our 0.5 M KCl electrolyte adjusted to pH 5.0). The galvanostatic charge/discharge curves recorded in this electrolyte (short-dashed red lines in Figure 2) present biphasic shapes that are reminiscent of those discussed above for the unbuffered NH$_4$Cl electrolyte. The main difference is the higher charge required to reach the stationary regime ($Q_c > 20$ mA·h/g), as well as the shift to more negative potentials. This larger potential shift clearly attests to the requirement for more negative potentials to efficiently insert protons in TiO$_2$ in this electrolyte (indicating a thermodynamic cost to proton insertion from water), which also implies that the local pH evolves towards more basic values than the previously discussed electrolytes. Since the H$_2$O/OH$^-$ couple is now involved in the electrochemical reaction, the local pH should satisfy the following expression:

$$pH_{z=0} = 14 + \log\left(\frac{|i|\delta_{max}}{FSD_{OH^-}} \right) \tag{12}$$

Assuming $D_{OH^-} = 5.3 \times 10^{-5}$ cm^2/s,[12] a δ_{max} value of 430 μm can be estimated, which leads, using **equation 12**, to a local pH value of 12.5. This value, although a little higher than the estimate from Figure 2C (*i.e.*, pH 11.1), remains consistent with our expectations. In the subsequent discharge, similar to the behaviour in the NH$_4$Cl electrolyte, we first observe a near-linear and rapid decrease of the potential, indicating a drastic reversal of the local pH to acidic values. Next, the potential evolves more slowly and finally superimposes on the discharge curve previously recorded in the NH$_4$Cl electrolyte (therefore suggesting the same pH$_{z=0}$ ~2.5 at the end of the discharge in both unbuffered electrolytes).

To confirm the significant pH change at the electrode/electrolyte interface, we performed galvanostatic experiments coupled with a UV-vis readout to monitor the absorbance change *in situ* (in transmittance mode) at a transparent GLAD-TiO$_2$/FTO electrode during cycling. To reveal the pH variation, a small amount of phenolphthalein (0.5 mM) was added to the electrolyte (0.3 M KCl), which, according to its pK_a of 9.4, changes from colorless to pink above pH 9.4. The galvanostatic cycles with simultaneously recorded absorbance (at 552 nm, corresponding to the maximum absorbance of the phenolphthalein's conjugate base) are shown in **Figure 3**. In these experiments, the charge was limited to 50 mA·h/g (*i.e.*, $x = 0.15$) to avoid both interference from HER as well as irreversible damage of the underlying FTO substrate during cycling at excessively negative potentials and slow rates. The charge and discharge curves show biphasic profiles similar to those obtained previously in 0.5 M KCl, indicating the absence of phenolphthalein interference in the charge storage (compare the magenta and dashed red curves in Figure 3 and see the associated comment in the SI).

It is interesting to note that the absorbance trace also exhibits a biphasic shape, implying two distinct contributions. The first absorbance contribution is attributed to the blue coloration of TiO$_2$ related to electrochemical doping,[[18]] which appears in the data as a nearly linear and symmetrical increase/decrease of absorbance during the galvanostatic cycle (an identical trace is recorded in the phenolphthalein-free electrolyte, see dashed red line in Figure 3).

A second absorbance contribution is observed after a lapsed time > 40 s (equivalent to $Q_c > 15$ mA·h/g), which is not observed in the phenolphthalein-free electrolyte nor in the buffered acetate electrolyte with phenolphthalein (grey line in Figure 3). This second contribution thus signals the accumulation of the pink deprotonated form of phenolphthalein at the electrode interface due to the local pH increase stemming from proton insertion and concomitant hydroxide production (equation 10). In contrast, the lack of pink coloration (and thus of significant proton insertion) during the early stage of the charge process (*i.e.*, the initial 40 s) points to a different charge storage mechanism that we attribute to the charging of the electrode double-layer capacitance (*vide infra*). In addition to the spectroelectrochemical experiment, the local change in coloration upon cycling was filmed (see Movie S1 in SI). The front-view images of the electrode taken at different time intervals upon charge (Figure 3) show a homogeneous pink colour on the whole electrode surface. In addition, side-view images confirm that the pink layer initially develops in the immediate vicinity of the electrode and then gradually extends into the bulk electrolyte, normal to the electrode. All this confirms that the pH near the electrode increases by several units, well above pH 9.4. The progressive spatial extension of the pink layer is also fully consistent with the time course growth of the OH$^-$ diffusion layer, reaching
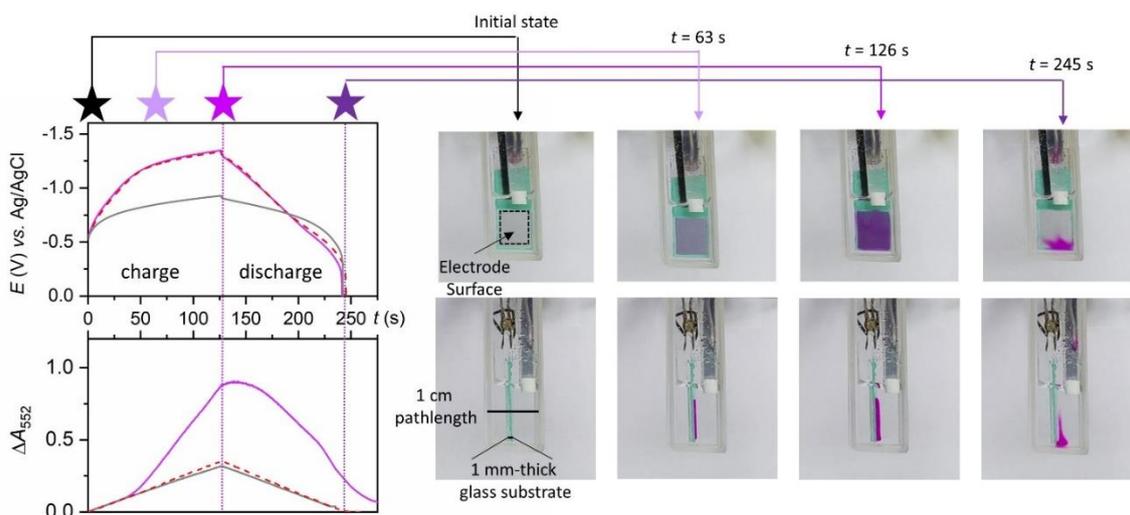
Figure 3. Left: (top) charge/discharge curves and (bottom) concomitant absorbance changes (measured at 552 nm) recorded during the galvanostatic cycling (rate: 0.36 mA/cm^2) of a GLAD-TiO$_2$/FTO electrode in: (magenta) an unbuffered aqueous electrolyte (0.3 M KCl adjusted to pH 5.0) containing 0.5 mM phenolphthalein, (grey) a buffered acetate electrolyte (1 M, pH 5.0) containing 0.5 mM phenolphthalein, and (dashed red lines) an unbuffered aqueous electrolyte (0.3 M KCl adjusted to pH 5.0) without phenolphthalein. The charges were all limited to 50 mA·h/g (equivalent to 126 s). Right: photographs of the spectroelectrochemical cell recorded (top) perpendicular or (bottom) lateral to the GLAD-TiO$_2$ electrode and at different time intervals (marked at the top of the figure) during cycling in the unbuffered aqueous electrolyte containing 0.5 mM phenolphthalein.

up to ~0.10-0.12 cm at the end of charge. During the subsequent discharge, the absorbance at 552-nm decreases nearly linearly and almost back to zero. On the image taken at the end of the discharge process (*i.e.*, at $t = 245$ s), we indeed notice that the transparency is entirely recovered within a well-defined thin layer formed close to the electrode surface, while a residual pink coloration persists in the bulk electrolyte with convective swirls moving to the cell bottom. This residual pink colour is characteristic of the hydroxide ions lost by natural diffusion-convection, which is also driven by buoyancy effects (*i.e.*, resulting from the small local variation of the electrolyte density which, under gravitational force, leads to a displacement of the more basic electrolyte towards the cell bottom – *vide infra*).[15] These results provide compelling evidence of the strong pH gradients which develop at the TiO$_2$ electrode interface. This also unambiguously confirms that we are dealing with a proton insertion-coupled charge storage mechanism, wherein water plays the triple role of solvent, charge carrier and proton donor, as illustrated in equation 10.

We next conducted a quantitative study of the dynamics of the pH gradient from analysis of the pink propagation front in the side-view video (Movie S1 in SI). The video images were

processed to extract the RGB intensities of each pixel (see Experimental Section), which range from zero to 255. Then, the intensity of the green component was analysed within a small 0.64×0.05 cm^2 area (as shown by the grey box in **Figure 4A**) encompassing the electrode (localized
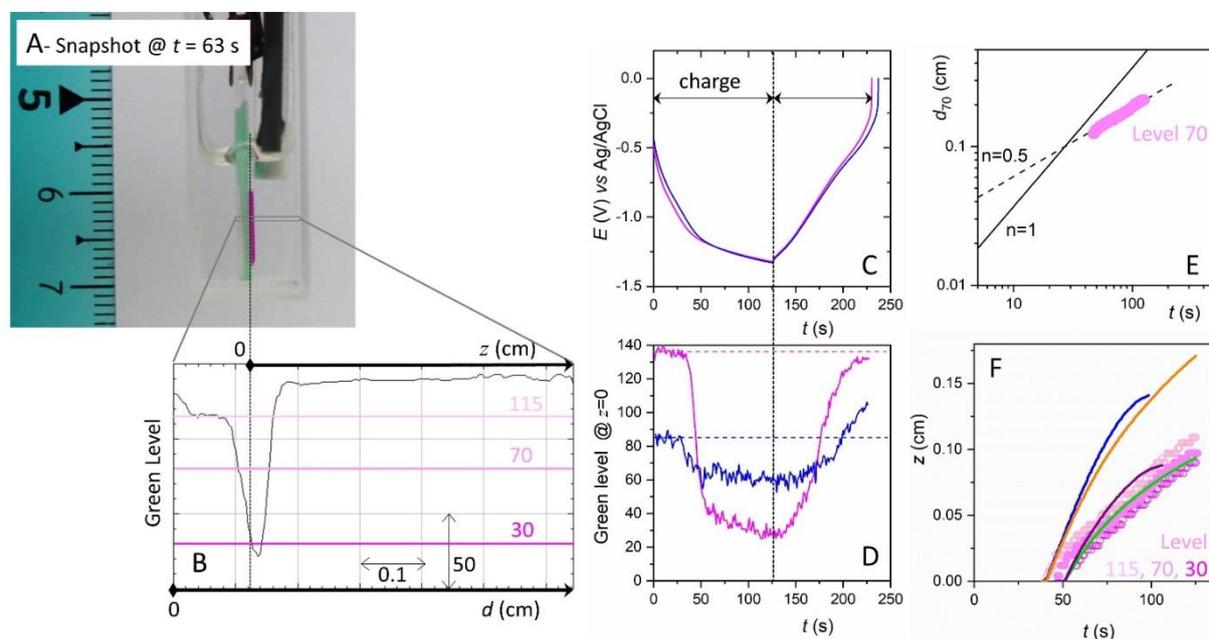

Figure 4. Analysis of the propagation rate of the pink or blue-green color fronts generated during the charge/discharge cycle (rate: 0.36 mA/cm^2; charge time: 126 s) of a GLAD-TiO$_2$/FTO electrode in an unbuffered aqueous electrolyte (0.5 M KCl) containing either 0.5 mM phenolphthalein or 0.7 mM bromocresol green as pH indicator. (A) Snapshot extracted at $t = 63$ s from the Movie S1 in SI obtained in the presence of phenolphthalein. (B) Grey level profile extracted (along the side-view section marked by the grey box in A) from the Movie S2 in SI. (C) Galvanostatic cycles recorded in the presence of either (pink) phenolphthalein or (blue) bromocresol green, and (D) their corresponding time-dependence grey level at $z = 0$. (E) Log-log scale of the time courses of the pink color propagation front distance (extracted from the grey level 70 on the Movie S2 in SI), taking as reference distance d the left end of the grey box in A. (F) Normal scale of the time course of the pink color propagation front distance (extracted from the grey levels 115, 70 and 30, which is equivalent to going from light to dark pink), taking as reference distance the metal oxide/electrolyte interface (*i.e.*, $z = 0$ cm). The solid lines represent the theoretical time course of the pH 9.4 position normal to the electrode (*i.e.*, in the z direction) computed from simulation of the (orange, green) 1D or (blue, purple) 2D model and considering (green, purple) or (orange, blue) not the contribution of phenolphthalein.

at a distance $d = 0.12$ cm from the left side of the analysis area, see Figure 4B) and electrolyte domains. Initially, the electrolyte was completely transparent and the green intensity level was ~140 in the whole analysed area, and once the pink colour appeared, the intensity of the green

channel decreased as the coloration became more intense. From these data (see Movie S2 in SI and samples shown in Figure S3), we first examined the time-dependence of the green level at the electrode/electrolyte interface (*i.e.* at $z = 0$, Figure 4D). We observed a consistent green intensity of ~140 for the first ~40s, then as the pink coloration appears, the green level at $z = 0$ decreased rapidly to 40 and then more slowly until it reached 20 at the end of the charge process. During the subsequent discharge, the green level at $z = 0$ gradually increases back to ~140. These observations, consistent with the previous data, are indicative of a significant upshift/downshift in $pH_{z=0}$ during the charge/discharge processes, with a value >> 9.4 at the end of charge and << 9.4 at the end of discharge.

Next, we analysed the propagation rate of the pink colour front in solution. For that purpose, we selected a green level of 70, which corresponds to half its maximal change (Figure S3), and we assumed that this corresponds to a ~ 1:1 ratio between the acid and base states of phenolphthalein and thus a local pH of ~9.4. During the first 45 s, the green level at $z = 0$ remains > 70, indicating a $pH_{z=0}$ < 9.4 (Figure 4D). After that, the green level at $z = 0$ further decreases, while the spatial extent of the area with green level < 70 expands until the end of charge (see Figure S4 as well as Figures 4A and 4B, where a value of z_{70} ~ 0.03 cm is reached after 63 s). In Figure 4E the raw d_{70} value ($d_{70} = z_{70} + 0.12$ cm) is plotted on a log-log scale as a function of charging time. The d_{70} scales almost linearly with the square root of time over much of the charging process, indicating that the progress of the pH 9.4 front is initially diffusion limited.

The pH front experiment was also repeated using bromocresol green as an alternative colorimetric pH indicator (see Movie S3 in SI). The electrolyte was initially adjusted to pH 5, which is close to the pK_a value (*i.e.*, 4.7) of bromocresol green so that it partitions between acidic (yellow) and basic (blue) forms, with a ratio close to 1:1. This produces a homogeneous blue coloration of the electrolyte (see Figure S4) that results in a starting green level of ~85. After a short delay, a darker blue layer develops at the electrode/electrolyte interface during charging, signalling a local pH increase. As this happens, the grey level at $z = 0$ decreases to a stable value of ~60 (see blue plot in Figure 4D). During the ensuing discharge process, the green level reverses to its initial value after 200 s and then continues to increase to a maximal value of ~105 at the end of the discharge, reflecting significant local acidification of the electrolyte. In the images extracted at the end of the discharge (see Figure S6), one can indeed notice the appearance of a thin light yellow layer at the electrode/electrolyte interface, indicating the local predominance of the acid form of the indicator, and confirming that a $pH_{z=0}$ << 4.7 is reached

at the end of the discharge process. This observation is in agreement with the local pH we estimated above (~2.5) from the potential measured at the end of discharge process.

2.5. Modelling/simulations of the galvanostatic curves

To move to a more quantitative analysis of the galvanostatic curves under buffered and unbuffered conditions, and also to predict and visualize the pH gradients which develop at the GLAD-TiO$_2$/electrolyte interface, we simulated the transport-reaction processes during a galvanostatic cycling experiment. To do so, we modified our previous two-compartment 1D model[22] to account for all acid-base equilibrium reactions in the electrolyte as well as all PICET reactions at the electrode interface, regardless of buffered or unbuffered electrolyte conditions (see SI for details). We also incorporated the capacitive contribution to the charge storage in the model. Furthermore, in order to facilitate the convergence of the numerical simulations, we assumed that the migration/diffusion of protons within the bulk TiO$_2$ is not rate-limiting due to the relatively slow charge/discharge rates used. This allowed us to simplify the previous two-compartment 1D model into a one-compartment 1D model, wherein TiO$_2$ is considered as a zero-dimensional film characterized by a maximal surface concentration Γ_O^0 (in mol per cm^2 of geometrical electrode area) of reducible Ti^{IV} centres (see SI for details). Finally, because of the slow rates that leave time for natural convection to interfere, we added a convection term to the mass transport equations of the electrolyte compartment (see SI for details). The model was solved numerically by a finite difference method implemented in the software Comsol Multiphysics (see SI). We first attempted to simulate the galvanostatic charge/discharge curves in buffered electrolytes at different pHs. The experimental parameters of the simulations were therefore modelled on those used to plot the curves in Figure 2 (including buffer concentrations, pH, charge/discharge rate, etc.). The others parameters such as the buffer pK_as and diffusion coefficients of the species in solution were recovered from literature, while those associated with the TiO$_2$ film were adapted from previous publications (see Table S1 in SI).[22] Because the heterogeneous rate constants (k_i^0) of PICET reactions associated with the different proton donor/acceptor couples were unknown, they were considered to be the same as the values previously determined in acetate buffer.[22] This approximation is justified since interfacial PICET kinetics are not rate-determining under the selected experimental conditions. The simulated galvanostatic charge/discharge curves (shown in Figure 2D and 2E) under both buffered and unbuffered conditions reproduce the shape, positioning and hysteresis of the experimental curves. The main difference lies in the more pronounced biphasic behaviour of the simulations, especially under buffered conditions. From

17

the simulations, we were able to disclose that the potential and time position of this biphasic transition varied with the differential double-layer capacitance of the film (*i.e.*, appearing earlier as C_{dl} decreases). This lead us to conclude that this biphasic transition signals the shift from capacitive charge storage (which leads to a rapid change in potential at the early stage of the charge process) to faradic proton insertion charge storage (which prevails after a given voltage, and translates into a tilted voltage plateau until TiO_2 is completely reduced). Experimentally, this transition is hardly visible in buffered media, but much more apparent in unbuffered media. The large voltage hysteresis simulated for the two unbuffered electrolytes (*i.e.*, the NH_4Cl and KCl aqueous electrolytes) are also in good agreement with those obtained experimentally, attesting to the strong local pH variations. These local pH changes were confirmed by plotting the simulated local pH (at $z = 0$) as a function of time and comparing it with that simulated for a buffered electrolyte of pH 5.0 (**Figure 5**), corroborating the pH changes assessed graphically from Figure 2. It is also interesting to note that during the charging process, the simulated pH variation only takes place after a certain delay, which corresponds to the time necessary for the potential to reach a sufficiently negative value so that, thermodynamically, the faradic PICET reaction *via* water or NH_4^+ sets in. During this delay, the charge storage is mainly capacitive in nature and thus proportional to the TiO_2 film capacitance. This also explains the lack of coloration in the early stage of charging performed in the presence of phenolphthalein (see Figure 4D).

It was next interesting to verify to what extent simulations can reproduce the colour front propagation (or pH gradient front) observed in Figure 3 and 4. For such purposes, we extracted the pH profiles across the *z*-coordinate as a function of time from the 1D simulation in KCl (Figure S5). The results reveal that strong pH gradients develop within the diffusion-convection layer and propagate normal to the electrode, which is qualitatively in good agreement with the experimental results in Figure 4. However, from a more quantitative point of view, we can see that the simulation leads to a larger pH front propagation distance in the electrolyte (reaching ~1.7 mm for pH 9.4 at the end of the charge process) than that obtained experimentally in Figure 4F (~1.1 mm at the end of the charge process − see also the orange simulated plot which is shifted to shorter time and over larger distance with respect to the experimental analogue). We suspected that this discrepancy might be due to phenolphthalein, which, because of its weak
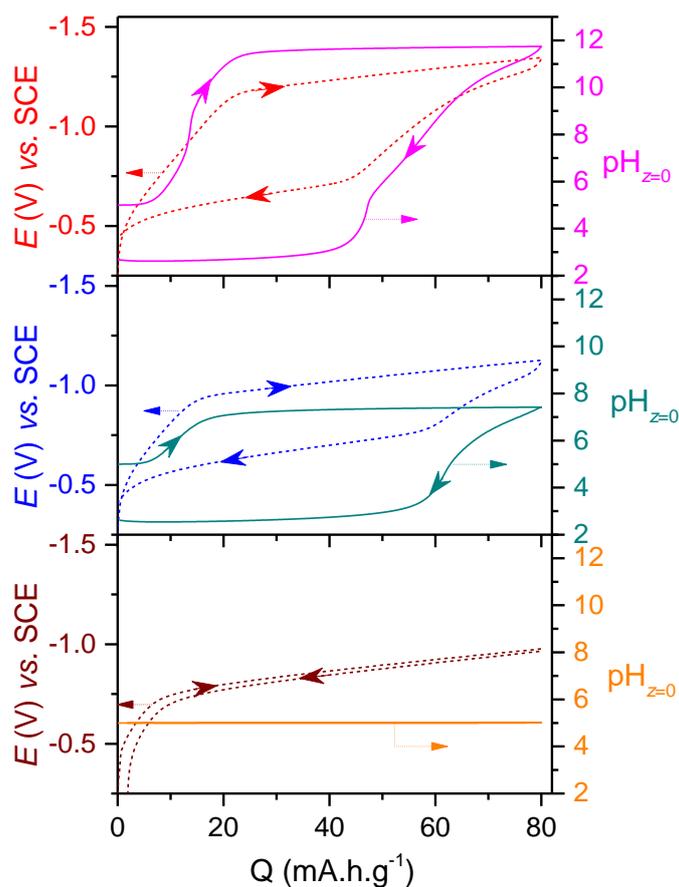
Figure 5. Theoretical (dashed lines) potentiometric plots and (solid lines) local pH changes numerically simulated (from the one-compartment 1D model) for galvanostatic charge/discharge cycles performed in unbuffered electrolytes (pH initially adjusted to 5.0) of (top) 0.5 M KCl and (middle) 0.4 M NH_4Cl, or in a buffered electrolyte of (bottom) 1 M acetate buffer (pH 5.0). The rate (0.36 mA/cm^2) and maximal charge (80 mA·h/g) are the same as for the experiments in Figure 2, while the other simulation parameters are gathered in Table S1.

acidity, may contribute to a partial neutralization of the electrogenerated OH⁻. We therefore incorporated phenolphthalein into the 1D model as an additional AH/A⁻ couple so that it could contribute to the various acid/base equilibria in the electrolyte and serve as a proton donor at the TiO_2 electrode interface. The simulations obtained under these conditions (Figure S5B) show a much better agreement with the experimental data, especially regarding the distance of 1.2 mm now reached by the pH 9.4 position at the end of charge process (green curve in Figure 4F), close to that obtained experimentally.

With our one-compartment 1D model, natural convection is only treated in an approximate way (by simply assuming a convection velocity vector oriented normal to the electrode), while in reality it is mainly induced by the local variation of the electrolyte density due to the change of concentration and nature of ions in the vicinity of the electrode, and leading to buoyancy-driven

convection effects. In the KCl electrolyte, one can understand that the OH$^-$ electrogenerated during charging increases the local density of the electrolyte, while during discharge, their neutralization in the diffusion-convection layer leads to the opposite effect. To account for this buoyancy-induced convection in the simulations, we extended the one-compartment 1D model to a one-compartment 2D model in which the normal velocity convection vector was replaced by 2D laminar flow fluid dynamics (allowing the effect of the local electrolyte density changes on the liquid dynamics to be simulated through the use of the Navier-Stokes continuity equation for an incompressible Newtonian fluid – see SI and Figure S6 for details). **Figure 6** shows the simulated 2D maps (at different time intervals) of the (*i*) pH gradient, (*ii*) pH gradient ≥ 9.4 (*i.e.*, the pH areas where phenolphthalein turned pink), (*iii*) electrolyte velocity field, and (*iv*) electrolyte density which develops across the electrochemical cell during a galvanostatic charge/discharge cycle in an unbuffered 0.5 M KCl electrolyte (the complete simulated datasets are also provided as videos S4 to S7 in the SI). At the beginning of the charge process, the lack of spontaneous convection in the cell results in a conventional linear mass-transport of the hydroxide ions, normal to the electrode (*i.e.*, in the *z*-direction – see Figure 6B). However, as the amount of released OH$^-$ near the electrode increases and densifies the electrolyte, a movement of the liquid to the cell bottom (*i.e.*, in the *y*-direction – see Figure 6D) is gradually initiated under the effect of gravity (note that this liquid drag-out effect is induced by a very small (<0.01%) change in the electrolyte density, Figure 6E). During the discharge, the electrolyte density is reduced, and the buoyancy effect slows then stops, resulting in the build-up of a significant amount of hydroxide ions at the cell bottom. The simulated pH map ≥ 9.4 (orange-red pattern in Figure 6C) reflects quite closely the density driven convection experimentally visualized in Figure 3 through the pink coloration of phenolphthalein (compare also Movie S1 and S5 in SI), including the spatial distribution of this coloration with the formation of swirls near the cell bottom. The maximal thickness of ~1.0 mm reached by the pH front ≥ 9.4 at the end of the charge process (Figure S5C and 6C) is also close to the ~1.1 mm value obtained experimentally (Figure 4F). The excellent agreement between simulations and experiments definitely supports our interpretation of the results and demonstrates the viability of quantitative prediction of the shape of galvanometric charge/discharge curves associated with the bulk reversible insertion of protons in a metal oxide such as TiO$_2$, and this is true in both buffered and unbuffered aqueous electrolyte media. The simulations also confirm that in unbuffered electrolytes, strong pH gradients develop at the electrode interface as a consequence of proton insertion. Finally, these results teach us that natural convection induced by local changes in electrolyte density also plays a role in the dynamics of charge carrier transport.
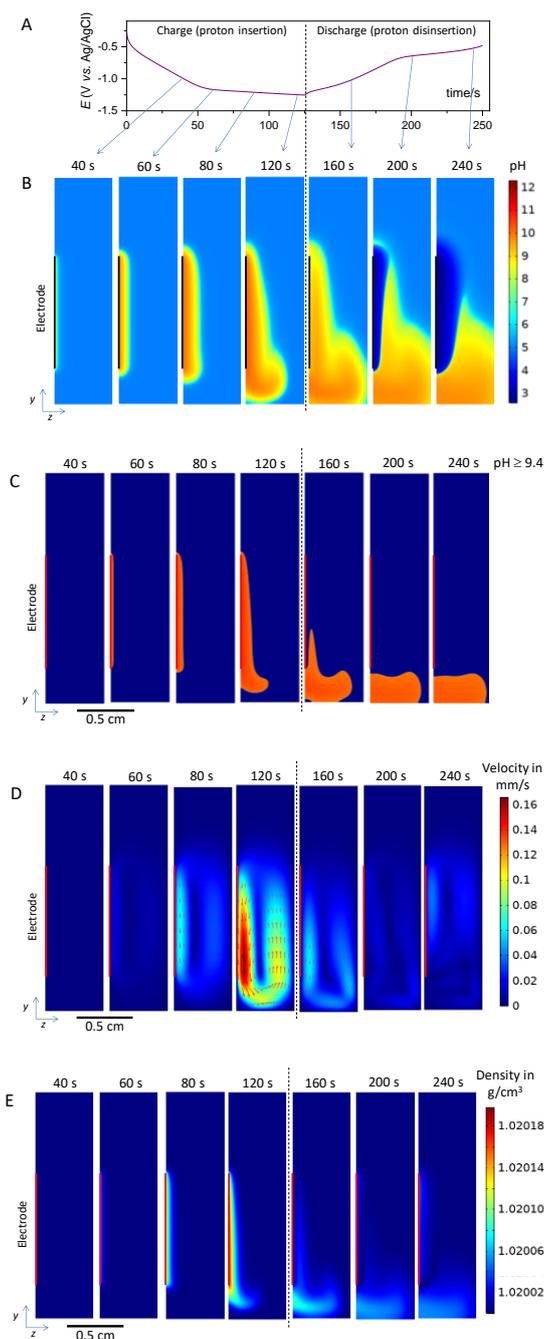
Figure 6. (Left) 2D simulations of (A) the galvanostatic charge/discharge curve, (B) electrolyte pH gradient map, (C) electrolyte pH gradient map for pH $\geq$ 9.4 (regions with pH <9.4 shown in uniform dark blue colour), (D) electrolyte velocity map (arrows represent the velocity vectors), and (E) electrolyte density map generated in a geometric cell configuration similar to the experimental one (see Figure 3) and using same conditions, *i.e.* a 0.5 M KCl aqueous electrolyte containing 0.5 mM phenolphthalein ($\rho = 1.02$ g/mL), a rate of 0.36 mA/cm^2, and a fixed charge/discharge time of 125 s (*i.e.*, 50 mA·h/g). The parameters used for the simulations are reported in Table S1.

3. Conclusion

Using nanostructured GLAD TiO$_2$ films as model electrodes capable of reversibly inserting 1 e$^-$/1 H$^+$ over the entire pH-range of water, we here provide decisive new insights into PICET in mild unbuffered aqueous electrolytes. In particular, we were able to clearly establish that the nature of the soluble species involved in the PICET reactions could vary during the electrochemical process due to the strong pH gradients which develop at the electrode/solution interface. This manifests on the galvanometric charge/discharge curves by the presence of significant voltage hysteresis, which directly depends on the pK_a values of the different proton donor/acceptor couples involved in the PICET process. These findings are of prime importance not only for aqueous rechargeable batteries in general, but also for energy conversion technologies involving electrode materials capable of inserting protons. Having here established efficient PICET with water as a proton donor, this contribution must definitely be considered when operating with insertion materials in aqueous electrolytes (or organic electrolytes containing a small amount of water). This has even broader prospects bearing in mind that some cationic charge carriers themselves exhibit weak Brønsted acidity, such as NH$_4^+$ (yet recently proposed as a non-metallic insertion charge carrier in several reports[40]) or multivalent cations solvated by water.[20] Indeed, owing to their stronger Brønsted acidity compared to water, these charge carriers are preferentially involved in PICET reactions, leading to distinct electrochemical features as established in the present study. It is moreover worth noting here the recently growing body of works concluding on a PICET charge storage mechanism from mild Al^{3+}-, Zn^{2+} and Mg^{2+}-based aqueous electrolytes and the use of electrode materials ranging from metal oxides[41–43] to non-oxide materials.[44–48]

Overall, the present study provides a comprehensive overview of the consequences of PICET in unbuffered mild aqueous electrolytes that can be easily generalised to other proton-insertion electrode materials. It also highlights the benefit of using buffered electrolytes for optimized energetic efficiency of PICET-based charge storage in mild aqueous electrolytes.

4. Experimental Section/Methods

Chemicals. Acetic acid (Reagent plus, >99%), sodium acetate, KCl (GR grade), ethanol absolute (EMSURE), and phenolphtalein were purchased from Sigma-Aldrich/Merck. Acetone (Normapur) was purchased from VWR Chemicals. Nafion D-520 dispersion and 1-propanol were purchased from Alfa Aesar. Bromocresol green (0.02% in aqueous solution) was purchased from Kuhlmann. FTO substrates (14 Ω/□) were purchased from Delta Technologies.

All aqueous solutions were made with deionized water (18.2 MΩ·cm) prepared with a TKA MicroPure UV purification system.

Electrode cleaning and modification. Prior to use, electrodes were cleaned in an ultraviolet ozone cleaner (UV/O$_3$ Procleaner™ plus, Bioforce Nanosciences) for 15 min and subsequently soaked at room temperature in acetone and then ethanol for 15 and 30 min, respectively. The electroactive GLAD-TiO$_2$ surface was delimited by depositing nail vanish to define a rectangular geometric electrode area, *S*, of 0.56 cm^2. GLAD-TiO$_2$/Ti electrodes were further modified with a Nafion™ coating to improve their cyclability. Briefly, a Nafion™ D-520 dispersion, 5% w/w in water and 1-propanol, was diluted in mixture of water and ethanol (50%:50%) in a 1 to 3 volume ratio. 20 µL of this mixture was deposited on the delaminated electrode surface and left to dry for 30 min in ambient air at room temperature, prior to electrode use. For spectroelectrochemical studies, the GLAD-TiO$_2$/FTO electrodes were used without Nafion coating to avoid pre-concentration of the colorimetric indicators in the polymer.

Electrochemical characterization. Cyclic voltammetry and galvanostatic cycling experiments were performed at ambient temperature in a three-electrode configuration using a VSP BioLogic potentiostat controlled by EC-Lab software. The counter electrode was a platinum wire and the reference electrode was a saturated calomel electrode (SCE, 0.242 V *vs*. NHE). The electrolyte was carefully degassed with argon for 20 min and a constant argon flow was kept above the electrolyte during the entire experiment to avoid faradaic currents arising from O$_2$ reduction during proton insertion. In CV, a systematic Ohmic drop compensation was performed. The current density was calculated from the current intensity normalized against the geometrical surface area, *S*, of the electrode.

The aqueous electrolytes used in the present study were as follows:

1- For buffered electrolytes, the total buffer concentration (acid + base) ranged from 0.35 to 1 M, and KCl was added when necessary to adjust the ionic strength to a minimal value of 0.5 M. The concentration, nature and pH of the buffered electrolytes were as follows: 1 M acetate buffer (pK_a = 4.76) at pH 5.0, 0.75 M HEPES buffer (pK_a = 7.5) at pH 7.9, 0.4 M ammonia buffer (pK_a = 9.25) + 0.5 M KCl at pH 9.1, 0.35 M CAPS buffer (pK_a = 10.4) + 0.65 M KCl at pH 9.8, and 0.5 M KPi buffer (pK_a = 12.3) at pH 12.2.

2- For unbuffered electrolytes, two solutions were studied: 0.4 M NH$_4$Cl + 0.5 M KCl, and 0.3-0.5 M KCl. For both electrolytes, the initial pH was adjusted to 5 by addition of diluted HCl.

3- For spectroelectrochemistry and videos, two electrolytes were studied: 0.5 mM phenolphthalein + 0.3-0.5 M KCl in an EtOH:H$_2$O 1:9 solution, and 0.7 mM bromocresol green

+ 0.3-0.5 M KCl. All electrolytes were initially stabilized at pH = 5 by addition of 1 mM acetate buffer.

Spectroelectrochemistry. Galvanostatic cycling experiments were conducted in a modified UV-visible cuvette using a Metrohm Autolab potentiostat controlled by GPES software. The potentiostat was synchronized with a UV-visible spectrometer (Torus, Ocean Optics) equipped with DH-2000-BAL light source (Ocean Optics). The counter electrode was a Pt wire isolated from the solution by a ceramic separator, and the reference electrode was an Ag/AgCl/sat. KCl electrode (DriRef 2, WPI Instrument, $E = 0.2$ V vs. NHE). The absorption was monitored in transmission mode, and for each spectrum presented as data, 50 individual spectra collected with accumulation times of 4 ms were averaged (the effective integration time was thus 0.2 s).

Video recording and data analysis

Side-view videos of the spectroelectrochemical cell were recorded in macro mode, using a Canon EOS 550D camera on a fixed stand. The image resolution was 1920×1080 pixels, and time resolution was fixed to 25 images/s. Using VLC software, we extracted 1 image/s of the video, and these frames were analysed with the splitchannel colour tool of the ImageJ2 software,[49] in order to extract the RGB components (with 8-bit encoding, corresponding to color levels ranging from zero to 255).

Supporting Information

Glossary of symbols, description of 1D and 2 D models, procedure for numerical simulations, estimation of the local pH on the basis of a simple linear diffusion-convection model, Table S1, Figures S1 to S6, and Movies S1 to S7. Supporting Information is available from the Wiley Online Library or from the author.

Acknowledgements

References

[1]   R. Demir-Cakan, M. R. Palacin, L. Croguennec, *J. Mater. Chem. A* **2019**, *7*, 20519.

[2]   D. Chao, W. Zhou, F. Xie, C. Ye, H. Li, M. Jaroniec, S. Qiao, *Sci. Adv.* **2020**, *6*, eaba4098.

[3]   D. G. Nocera, *J. Am. Chem. Soc.* **2022**, *144*, 1069.

[4]   M. T. M. Koper, *Chem. Sci.* **2013**, *4*, 2710.

[5]   P. Ruftschi, *J. Power Sources* **1977**, *2*, 3.

[6]   P. Oliva, J. Leonardi, J. F. Laurent, C. Delmas, J. J. Braconnier, M. Figlarz, F. Fiévet, A. de Guibert, *J. Power Sources* **1982**, *8*, 229.

[7]   L. Zhou, L. Liu, Z. Hao, Z. Yan, X. Yu, P. K. Chu, K. Zhang, J. Chen, *Matter* **2021**, *4*, 1252.

[8]   Y. Xu, X. Wu, X. Ji, *Small Struct.* **2021**, *2000113*, 1.

[9]   I. Katsounaros, J. C. Meier, S. O. Klemm, A. A. Topalov, P. U. Biedermann, M. Auinger, K. J. J. Mayrhofer, *Electrochem. commun.* **2011**, *13*, 634.

[10]   G. K. H. Wiberg, M. Arenz, *Electrochim. Acta* **2015**, *159*, 66.

[11]   E. B. Carneiro-Neto, M. C. Lopes, E. C. Pereira, *J. Electroanal. Chem.* **2016**, *765*, 92.

[12]   V. Grozovski, S. Vesztergom, G. G. Lang, P. Broekmann, *J. Electrochem. Soc.* **2017**, *164*, E3171.

[13]   M. Qureshi, A. T. Garcia-Esparza, T. Shinagawa, P. Sautet, T. Le Bahers, K. Takanabe, *Sustain. Energy Fuels* **2018**, *2*, 2044.

[14]   N. Pande, S. K. Chandrasekar, D. Lohse, G. Mul, J. A. Wood, B. T. Mei, D. Krug, *J. Phys. Chem. Lett.* **2020**, *11*, 7042.

[15]   K. Obata, R. van de Krol, M. Schwarze, R. Schomäcker, F. F. Abdi, *Energy Environ. Sci.* **2020**, *13*, 5104.

[16]   V. J. Ovalle, M. M. Waegele, *J. Phys. Chem. C* **2021**, *125*, 18567.

[17]   K. Obata, F. F. Abdi, *Sustain. Energy Fuels* **2021**, *5*, 3791.

[18]   Y.-S. Kim, S. Kriegel, K. D. Harris, C. Costentin, B. Limoges, V. Balland, *J. Phys. Chem. C* **2017**, *121*, 10325.

[19]   Y.-S. Kim, K. D. Harris, B. Limoges, V. Balland, *Chem. Sci.* **2019**, *10*, 8752.

[20]   S. J. Hawkes, *J. Chem. Educ.* **1996**, *73*, 516.

[21]   M. J. Park, H. Y. Asl, A. Manthiram, *ACS Energy Lett.* **2020**, *5*, 2367.

[22]   N. Makivic, J.-Y. Cho, K. D. Harris, J.-M. Tarascon, B. Limoges, V. Balland, *Chem. Mater.* **2021**, *33*, 3436.

[23]   L. A. Lyon, J. T. Hupp, *J. Phys. Chem. B* **1999**, *103*, 4623.

[24]   Y. Ma, X. L. Wang, Y. S. Jia, X. B. Chen, H. X. Han, C. Li, *Chem. Rev.* **2014**, *114*, 9987.

[25]   J. N. Schrauben, R. Hayoun, C. N. Valdez, M. Braten, L. Fridley, J. M. Mayer, *Science .* **2012**, *336*, 1298.

[26]   J. R. Swierk, N. S. Mccool, T. P. Saunders, G. D. Barber, T. E. Mallouk, *J. Am. Chem. Soc.* **2014**, *136*, 10974.

[27] Y. Kim, S. Kriegel, A. Bessmertnykh-lemeune, K. D. Harris, U. Claude, B. Lyon, *ChemElectroChem* **2021**, *8*, 2640.

[28] M. A. Spencer, J. Fortunato, V. Augustyn, *J. Chem. Phys.* **2022**, *156*, 064704.

[29] E. V Miu, J. R. McKone, G. Mpourmpakis, *J. Am. Chem. Soc.* **2022**, *144*, 6420.

[30] M. D. Levi, D. Aurbach, *Electrochim. Acta* **1999**, *45*, 167.

[31] D. R. Lide, Ed. , *CRC Hanbook of Chemistry and Physics*, CRC Press, Bocan Raton, FL, **2005**.

[32] C. Amatore, S. Szunerits, L. Thouin, J. S. Warkocz, *J. Electroanal. Chem.* **2001**, *500*, 62.

[33] M. Mateos, N. Makivic, Y.-S. Kim, B. Limoges, V. Balland, *Adv. Energy Mater.* **2020**, *10*, 2000332.

[34] J. Han, A. Varzi, S. Passerini, *Angew. Chemie - Int. Ed.* **2022**, *61*, e202115046.

[35] J. J. Holoubek, H. Jiang, D. Leonard, Y. Qi, G. C. Bustamante, *Chem. Commun.* **2018**, *54*, 9805.

[36] S. Dong, W. Shin, H. Jiang, X. Wu, Z. Li, J. Holoubek, W. F. Stickle, B. Key, C. Liu, J. Lu, P. A. Greaney, X. Zhang, X. Ji, *Chem* **2019**, *5*, 1.

[37] H. Li, J. Yang, J. Cheng, T. He, B. Wang, *Nano Energy* **2020**, *68*, 104369.

[38] G. Liang, Y. Wang, Z. Huang, F. Mo, X. Li, Q. Yang, D. Wang, H. Li, S. Chen, C. Zhi, *Adv. Mater.* **2020**, *1907802*, 1.

[39] Y. Song, Q. Pan, H. Lv, D. Yang, Z. Qin, M. Zhang, X. Sun, X. Liu, *Angew. Chemie - Int. Ed.* **2021**, *60*, 5718.

[40] G. Liang, F. Mo, X. Ji, C. Zhi, *Nat. Rev. Mater.* **2021**, *6*, 109.

[41] P. Oberholzer, E. Tervoort, A. Bouzid, A. Pasquarello, D. Kundu, *ACS Appl. Mater. Interfaces* **2019**, *11*, 674.

[42] Z. Li, S. Ganapathy, Y. Xu, Z. Zhou, M. Sarilar, M. Wagemaker, *Adv. Energy Mater.* **2019**, *9*, 1900237.

[43] Q. Zhao, L. Liu, J. Yin, J. Zheng, D. Zhang, J. Chen, L. Archer, *Angew. Chemie Int. Ed.* **2020**, *59*, 3048.

[44] M. J. Park, A. Manthiram, *ACS Appl. Energy Mater.* **2020**, *3*, 5015.

[45] Z. Tie, L. Liu, S. Deng, D. Zhao, Z. Niu, *Angew. Chemie - Int. Ed.* **2020**, *59*, 4920.

[46] Z. Tie, S. Deng, H. Cao, M. Yao, Z. Niu, J. Chen, *Angew. Chemie - Int. Ed.* **2022**, *134*, e202115180.

[47] Z. Lin, H. Shi, L. Lin, X. Yang, W. Wu, X. Sun, *Nat. Commun.* **2021**, *12*, 4424.

[48] A. I. Komayko, S. V Ryazantsev, I. A. Trussov, N. A. Arkharova, D. E. Presnov, E. E.

Levin, V. A. Nikitina, *ChemSusChem* **2021**, *14*, 1574.

[49] C. T. Rueden, J. Schindelin, M. C. Hiner, B. E. DeZonia, A. E. Walter, E. T. Arena, K. W. Eliceiri, *BMC Bioinformatics* **2017**, *18*, 529.